Experimental Mechanics (2022) 62:1163–1174
https://doi.org/10.1007/s11340-022-00866-2

RESEARCH PAPER

A Joule Heated High-Temperature Tensile Split Hopkinson Pressure Bar

A. Lew[1] · **O.T. Kingstedt**[1]

Received: 31 January 2022 / Accepted: 17 May 2022 / Published online: 16 June 2022

Abstract

Background Extreme application conditions frequently consist of environments involving one or more of the following factors: very high (or low) temperatures, irradiation, corrosive medium exposure, elevated stresses, and high-strain-rate loading. Due to challenges in replicating environments where more than one factor is present, experiments typically are restricted to investigating a single environmental condition.

Objective The objective of the efforts outlined herein is to demonstrate the precisely-controlled high-rate heating of a variety of metallic material systems up to one-half their melting temperature within a Tension Split-Hopkinson Pressure Bar (TSHPB).

Methods Specific materials investigated include Ti-6Al-4V, Inconel 718, and Magnesium alloy AZ31B. The adopted method integrates a duty-cycle controlled Joule heating system with a TSHPB system.

Results Accurate and repeatable heating profiles (i.e., within ±5 °C of the desired temperature up to 725 °C) allow testing without direct temperature monitoring. Combined, the Joule heating system and TSHPB provide an experimental setup capable of strain-rates up to $10^3\ s^{-1}$, a heating system that can produce currents up to $250\,A$, resulting in material-specific heating rates exceeding $100\,K/s$. Constraining heating times to a few seconds limits microstructural changes, thereby suppressing annealing or grain growth processes, resulting in unique, non-equilibrium superheated microstructure states.

Conclusion The presented system enables the study of elevated temperature high-strain-rate material behavior, which is relevant to improving understanding of material behavior during high-speed machining, forging, high-velocity vehicle crashes, protection system response to impacts and blast, as well as nuclear energy applications.

Keywords Tension Split-Hopkinson pressure bar · Kolsky bar · Dynamic behavior of materials · Elevated temperature · Joule heating

Introduction

The certification and adoption of materials for extreme environment applications requires understanding the effects of multiple factors (e.g., temperature and strain-rate) on material behavior. At elevated temperatures, time-temperature-dependent microstructural activation mechanisms (e.g., dislocation glide, twinning) can significantly impact a material's mechanical response. Elevated temperatures provide additional energy to aid mechanisms in overcoming activation barriers, reducing the driving stresses required for mechanism activity (e.g., [1]). For example, it has been shown that Ti-6Al-4V exhibits an 85% reduction in flow stress in quasi-static experiments conducted at temperatures nearing one-half of the melting temperature (T_m) compared to room temperature experiments [2]. Understanding and quantifying these temperature-dependent effects is necessary to accurately model and predict material behavior, which allows for improved efficiency in design and application. Similarly, transient activation mechanisms in materials cause changes in mechanical behavior at high-strain-rates. Dislocation slip follows the Arrhenius form for thermal activation mechanisms [3], such that the increased energy available to overcome to activation barrier is in the form of dislocation vibration induced by the vibration of surrounding atoms [4]. The vibrational energy is only useful when it acts in the direction of the energy barrier saddle [5], thus there are finite time periods when the vibrational energy cannot contribute to dislocation slip. At high-strain-rates, there is less time

✉ O.T. Kingstedt
o.kingstedt@utah.edu

[1] Department of Mechanical Engineering, University of Utah, Salt Lake City, UT 84112, USA

for a dislocation to move, decreasing the likelihood that the vibration is aligned with the Burgers vector during deformation. Misaligned vibrations will either require more energy to overcome the activation barrier for movement or will remain pinned during deformation, increasing the required flow stress at the onset of plasticity. For example, experiments conducted on 4340 steel have shown a 20% increase in flow stress at high-strain-rates ($\dot{\varepsilon} = 3.6 \times 10^3\ s^{-1}$) compared to quasi-static strain-rates ($\dot{\varepsilon} = 10^{-3}\ s^{-1}$) [6].

Both temperature and strain-rate affect the time-temperature dependent plastic activation mechanisms, with elevated temperatures lowering the effective activation barrier and high-strain-rates decreasing the time when these mechanisms can take effect. The interactions between the thermal activation and dislocation motion at high-strain-rates thus present an opportunity for further investigation. Understanding these effects is essential to model a material's mechanical behavior accurately. For example, machining processes often experience conditions of high-strain-rates at elevated temperatures due to adiabatic heating during cutting [7]. Other high-strain-rate processes like forming and rolling are intentionally performed at high temperatures to improve workability [1]. Further applications, especially in aerospace and nuclear industries, require materials to operate in high-temperature environments. High-strain-rate experimentation at elevated temperatures can provide the data required to model these processes accurately and predict the failure behavior of materials in the event of a crash or impact [8] or under seismic loading [9].

Currently, only a handful of experimental setups exist in literature that are capable of performing high-temperature, high-strain-rate experiments in tension on non-equilibrium, superheated microstructures without impeding the view of the specimen during loading. This unique combination of experimental parameters is essential to study thermomechanical material behavior in extreme environments or during dynamic processes. A variety of heated split-Hopkinson pressure bar (SHPB) systems exist. However, few are suited to performing experiments identical to those presented herein. As many materials exhibit loading orientation asymmetry, data gathered from compression SHPB systems cannot be relied upon to predict tensile behavior. Similarly, heating systems that have low heating rates (requiring long heating periods) cannot be used to study non-equilibrium microstructures that arise during dynamic processes. SHPB systems that are enclosed or otherwise obstruct specimen view cannot be used in conjunction with full-field imaging techniques (e.g., digital image correlation or the grid method) or direct temperature measurement during loading, making studies of non-uniform deformation, inverse constitutive parameter identification or Taylor-Quinney coefficient identification impossible. The system presented herein combines these necessary experimental capabilities and is compared with other high-temperature SHPB experimental apparatuses in the discussion.

Background

Using an SHPB, a material's stress-strain behavior can be quantitatively determined at strain-rates up to $10^3\ s^{-1}$. The original SHPB design allowed only for compression testing of materials [10]. Material behavior, however, is loading mode-dependent (e.g., tension vs. compression). Thus, it is critically important to be able to test materials in the loading mode in which they will be used to predict their behavior accurately. To enable the measurement of high-strain-rate tensile behavior, the classical SHPB design is modified [11]. In a Tension Split-Hopkinson Pressure Bar (TSHPB) experiment, the experiment is initiated when a tubular striker bar is launched via a gas gun, impacting a flange on the incident bar. The impact generates an elastic tension wave that propagates down the length of the incident bar toward the specimen. The specimen is mounted between the incident and transmitted bar using clamps that are threaded directly onto the bars to transmit the stress wave [12]. At the incident bar specimen interface, the acoustic impedance difference causes part of the tension wave to be reflected as a compression wave, while the remainder of the tension wave travels through the specimen. Similarly, at the specimen transmission bar interface, part of the wave is reflected back through the specimen, equilibrating the specimen's stress state. The remainder of the wave then travels through the transmission bar. Data from strain gauges on the incident and transmission bars and one-dimensional wave propagation theory is then used to calculate stress-strain curves [13].

The nominal specimen stress ($\sigma_s(t)$) can be calculated by dividing the force on the transmitted interface, calculated with the bar modulus of elasticity (E), measured transmitted strain ($\varepsilon_t(t)$), and the bar cross-sectional area (A_b), by the cross-sectional area of the specimen (A_s) [14], shown in equation (1),

$$\sigma_s(t) = \frac{E\,\varepsilon_t(t)\,A_b}{A_s}. \tag{1}$$

The nominal specimen strain ($\varepsilon_s(t)$) can be calculated based on the reflected pulse strain. The specimen strain is a function of bar wave speed (c_0), specimen length (L_s), the duration of the reflected pulse (t_r), the reflected pulse strain ($\varepsilon_r(t)$), and an incremental time step ($d\tau$) [14], shown in equation (2),

$$\varepsilon_s(t) = -\frac{2\,c_0}{L_s}\int_0^{t_r} \varepsilon_r(\tau)\,d\tau. \tag{2}$$

Further details on the data reduction in TSHPB experiments can be found in Ref. [13] and [14]. As shown in equations (1) and (2), the stress and strain calculations rely on the bar material behavior, specifically bar speed and modulus of elasticity. In room temperature experiments, the bar speed

and modulus can be treated as constant (such that the bars remain in the elastic region during loading [15]). In high temperature experiments, however, significant heating can occur in the bars, affecting bar behavior and experimental results. This effect can be accounted for in post-processing [16] or can be mitigated by minimizing bar end heating. In C350 Maraging steel (a common SHPB bar material which is used in this study), the decrease in bar speed caused by elevated temperatures only exceeds 5% at temperatures above 350 °C [17]. Similarly, the modulus of elasticity decreases by about 5% at temperatures exceeding 250 °C [18], and microstructural changes are negligible for short durations under 450 °C [19]. Thus, by ensuring the bar end heating remains below these temperatures, the temperature effect on the bar material behavior can be neglected.

Bar end heating can be reduced by actively cooling the bars [20] or by decreasing heat transfer into the bars (from direct heating or by conduction through the specimen). The latter can be accomplished with high heating rates to minimize the time the bars are in contact with the heated specimen and by ensuring heating is localized to only the gauge section of the sample. For the system presented in the following, the temperature rise of the bar end grip region is limited to $\leq$ 75 °C, even when specimen temperatures are an order of magnitude higher (750 °C). At sufficiently high heating rates, microstructural changes in the specimen are also negligible. Diffusion based microstructural changes (e.g., annealing, grain growth, recrystallization) take time on the order of minutes or hours to substantially affect the material behavior at temperatures up to half of a material's melting temperature for most metals [21]. By testing materials in superheated, non-equilibrium states, behavior during dynamic, quasi-adiabatic events such as machining and cutting can be studied. Other important considerations that must be taken into account when designing a heated TSHPB system include specimen temperature uniformity, heating precision, and specimen viewing. Uniformity and precision are necessary to understand the material response and ensure that the entire gauge section is deformed under the same conditions. An unobstructed view of the specimen throughout loading is desired for studies involving DIC and infra-red (IR) thermography.

To accomplish these goals in a heated TSHPB setup, a variety of heating methods have been used, including IR spot heaters, [1, 22] furnaces, [23, 24] pulse-heating systems [7, 25] and induction heating systems [26, 27]. IR spot heaters generate a high-intensity beam of IR radiation that is focused on a sample to cause heating. Spot heating SHPB systems' advantages include their simplicity and minimal bar end heating, but require direct temperature monitoring, can cause temperature gradients within the sample, and generally exhibit relatively low heating rates (on the order of tens of *K/s* [1]). Furnace-based heating systems enclose the specimen and bars in a furnace (electric tube and shell furnace [24] or focused halogen lamp radiant furnace [28]) to heat the specimen. These systems offer uniform heating but at relatively low rates (on the order of tens of *K/s* [24]) and lead to significant bar end heating. Though bar heating can be minimized by bringing the bars into contact with the specimen after heating, these actuation systems introduce complexity and can lead to specimen cooling before deformation. Pulse- or Joule heating utilizes resistive heating by directly passing current through a resistor (e.g., specimen). Joule heating can be localized in the material sample itself or in high-resistance inserts (graphite sheets in Ref. [7]) which conduct heat to the sample. Induction heating uses high-frequency alternating current in a coil that serves as the primary of a transformer to heat the secondary without contact. The heated secondary can be the sample itself (e.g., [26, 27]) or in the clamps which conduct heat into the sample (e.g., [20]). Heat energy is generated by the induced currents, again through resistive heating. Joule and induction heating systems offer relatively high heating rates on the order of hundreds [27] or thousands [7] of *K/s* (and low heating times), but can cause significant bar end heating, non-uniform temperature gradients, and electromechanical behavior effects.

These electromechanical effects include electroplasticity and electromigration. Electroplastic behavior occurs when high current densities during deformation contribute energy to dislocation movement, reducing the effective flow stress in a material [29]. The prevalence of electroplasticity and the required current densities vary by material, but can be mitigated by including a sufficient delay following the termination of current before loading. This delay will ensure residual electric fields and current can dissipate before deformation. Electromigration, caused by the athermal effects of kinetic energy from electron momentum [30], refers to the change in phase transformation behavior caused by an applied electrical current [31]. The additional energy supplied by the athermal effect can reduce the necessary annealing temperatures and times for recrystallization to occur [32], and has been shown to accelerate other (e.g., precipitation, grain growth, etc.) microstructural evolution mechanisms. The rate of acceleration depends on the material, current density, and current type (i.e., direct or alternating, continuous or pulsing), making its effect difficult to predict [31]. As these transformations still rely on temperature activated, diffusion-based processes, they can be mitigated by minimizing the time the specimen is held at high temperatures.

Macro-scale material behavior arises from microstructure. Dislocation density, crystal structure, size and density of precipitates, grain size, and grain orientation can all affect a material's mechanical properties, including ultimate strength, yield strength, ductility, fracture behavior,

plasticity mechanisms, and flow stress. In metals, microstructural properties can depend on thermomechanical history (hot or cold working, annealing, etc.), chemical constituents or alloying materials, metallurgical solutionizing and quenching, and exposure to corrosive environments. As demonstrated by the variety of factors, the development of processing methods to achieve a certain microstructure or behavior is a rich field of research and ongoing study, though the following discussion will be limited to general processes which could impact measured dynamic testing behavior. Temperature-dependent microstructural evolution and annealing are the most influential processes that could affect the presented study. Evolution includes microstructural changes involving grain growth, precipitation, crystallization, and phase transformations. Each of these mechanisms results from added atomic or molecular mobility owing to elevated temperatures. As discussed previously, thermal energy provides additional energy for atomic movement. In evolution, the remainder of the energy is provided by electrochemical gradients. The movement allows atoms to organize into stable, lower-energy configurations. Similarly, during annealing processes, induced stresses from dislocations provide energy for their movement and deconstruction at sufficiently high temperatures. The annealing process leads to lower dislocation density, allowing for easier movement of remaining dislocations, and a decrease in flow stress and increase in ductility. As these microstructural changes are all time and temperature dependent, they can be mitigated by minimizing the amount of time a metal is held at elevated temperatures. It is worth noting that some microstructural evolution can occur near instantaneously (e.g, precipitation in some stainless steel [33] and aluminum alloys [34]). These near instantaneous reactions would occur in any elevated temperature environment, and thus their effect on mechanical high temperature mechanical behavior would be observed during high temperature experimentation. By isolating temperature effects, experiments can better model machining and forming processes where heating and deformation occurs rapidly, preventing most significant forms of microstructural evolution.

Theory

Joule heating can be combined with a TSHPB system by integrating the specimen and clamping system of the bars into a Joule heating circuit. In this configuration, the specimen's small dimensions result in heating being concentrated in the specimen's gauge section. The governing equation for the heating of a solid is shown in Newton's heat equation, equation (3). Here, the temperature change (ΔT) is a function of the energy input (Q), the mass (m), and the specific heat capacity (C_p),

$$\Delta T = \frac{Q}{mC_p}. \tag{3}$$

Taking a time derivative of this equation yields the solid heating rate equation, equation (4), where the heating rate ($\dot{T}$) is proportional to the power ($\dot{Q}$),

$$\dot{T} = \frac{\dot{Q}}{mC_p}. \tag{4}$$

Watt's law describes the power dissipated through a resistor (i.e., the specimen) as a function of voltage (V) and current (I), shown in equation (5),

$$P = VI. \tag{5}$$

Ohm's law describes the voltage across a resistor in terms of current and resistance (R), shown in equation (6),

$$V = IR. \tag{6}$$

Substituting equation (6) into equation (5) yields Joule's Law, equation (7),

$$P = I^2R. \tag{7}$$

Substituting equation (7) into the solid heating rate equation (equation (4)) yields equation (8),

$$\dot{T} = \frac{I^2R}{mC_p}. \tag{8}$$

The equation for the resistance across a solid is shown in equation (9), as a function of length (L), resistivity (ρ), and cross-sectional area (A),

$$R = \frac{L\rho}{A}. \tag{9}$$

Substituting equation (9) into equation (8) yields equation (10),

$$\dot{T} = \frac{I^2L\rho}{mC_pA}. \tag{10}$$

Finally, substituting the mass, density (d), and specimen gauge section volume into equation (10) yields the Joule heating rate equation, equation (11),

$$\dot{T} = \frac{I^2\rho}{dC_pA^2}. \tag{11}$$

The Joule heating rate equation, equation (11), provides an estimate of the heating rate of a solid when the current passing through the object (I), material properties (ρ, d, C_p), and cross-sectional area (A) are known quantities. A Joule heating system can then be designed to provide a specific

Table 1 Material properties and heating rates for selected metals

Material	Resistivity, ρ	Density, d	Specific Heat, C_p	Heating Rate, $\dot{T}$
	$(\mu\Omega\, cm)$	(g/cm^3)	$(J/g\, K)$	(K/s)
Ti-6Al-4V	171 [35]	4.429 [36]	0.5443 [36]	365
Inconel 718	128 [37]	8.221 [36]	0.4187 [36]	191
Mg AZ31B	10.2 [38]	1.769 [36]	0.9944 [36]	29.8

current through a specimen to achieve a desired heating rate.

For a current of 250 A through the specimen's gauge section (with the geometry shown in Fig. 3), theoretical heating rates can be determined with the Joule heating rate equation, equation (11). The required material properties and calculated heating rates for several materials are listed in Table 1. Equation (11) considers perfect heating, ignoring thermal losses, for example, via conduction through the specimen clamps, resulting in the difference between the theoretical and experimental heating rates. Although the theoretical heating rates do not precisely predict experimental heating, theoretical calculations provide a reasonable estimate for initially calibrating the control system and estimating the upper limit of heating rates for different input currents.

Methods

Using long bars ($L/D = 192$ in the current design) to transmit strains into the specimen allows for precise measurement of loading during testing by minimizing radial nonuniformity in the propagating wave [13]. In addition, wave dispersion is reduced by applying copper pulse shapers to the incident bar flange [39]. Over the experiment duration, the profile of propagating waves is gathered using strain gauges attached at the mid-length position of the incident and transmission bars. The strain gauges on each bar are arranged in a full Wheatstone bridge configuration for the presented work. This configuration is selected as bar bending, Poisson effects, and lead wire resistance are automatically eliminated from measurements. The Wheatstone bridge signal is conditioned and amplified with a Dewetron amplifier and then recorded with an oscilloscope. A typical waveform from a room temperature tension experiment conducted with copper pulse shaping is shown in Fig. 1.

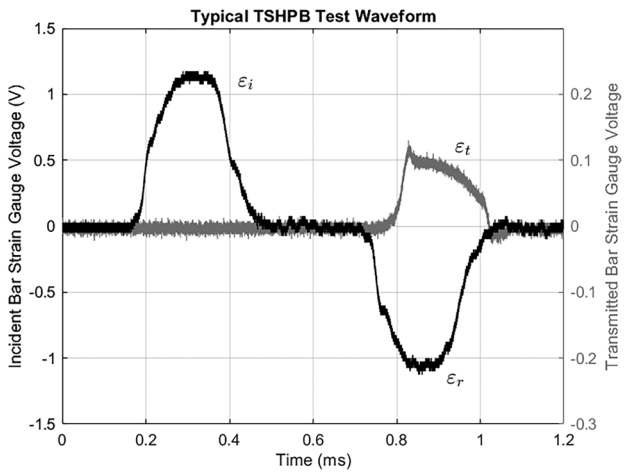

Fig. 1 Typical waveform from a pulse shaped TSHPB experiment

The High-Strain-Rate Mechanics of Materials Laboratory (HSRMML) at the University of Utah has a TSHPB system, shown in Fig. 2. Previous presentation of its design can be found elsewhere; see Refs. [40, 41]. The incident and transmission bars both have a diameter of 19.05 mm and a length of 3.66 m. Both ends of the incident bar have male 3/4"-16 threads. The striker end is threaded to attach an impact flange for the striker tube. The specimen interface of both bars are threaded to attach the specimen clamps. The specimen has a gauge length of 20.08 mm and a square cross-section with side length 3.32 mm. The specimen is held by the clamps with press-fit wedge grips purchased from REL Inc. The striker bar is accelerated with a gas gun, fired with a solenoid valve operated by the control system. The gas gun pressure is adjusted to achieve the desired strain-rates.

Figure 3 shows the nominal dimensions of the sample used for TSHPB testing in the HSRMML. Preliminary testing was completed with Ti-6Al-4V, Inconel 718, and Magnesium AZ31B. These materials exhibit a wide range of electrical resistivities, demonstrating the setup's broad material testing capabilities. In addition, these materials are often used in high-temperature applications (i.e., Ti-6Al-4V's use in intermediate compression stages in gas turbine engines and aircraft hydraulic tubing [42], and Inconel 718's use in later gas turbine engine stages and nuclear structure applications [43]) or display novel behavior in high-temperature machining processes (Magnesium AZ31B exhibits significant asymmetric yield conditions, and anisotropic hardening behavior [44]), making them ideal subjects for heated TSHPB studies.

An Arduino DUE-based control system regulates the main circuit used for heating, shown in Fig. 4. The Arduino DUE board is used to orchestrate testing because it has a simple, easy-to-edit interface and can send and receive analog voltage signals. The control system script directs the Arduino to send voltage signals to the Field Effect Transistor (FET) input circuit (see Fig. 5) to govern the specimen heating and to the solenoid control circuit (see Fig. 6) to fire the gas gun. The control system script calculates the duty cycling for heating and sets the delay following heating. An

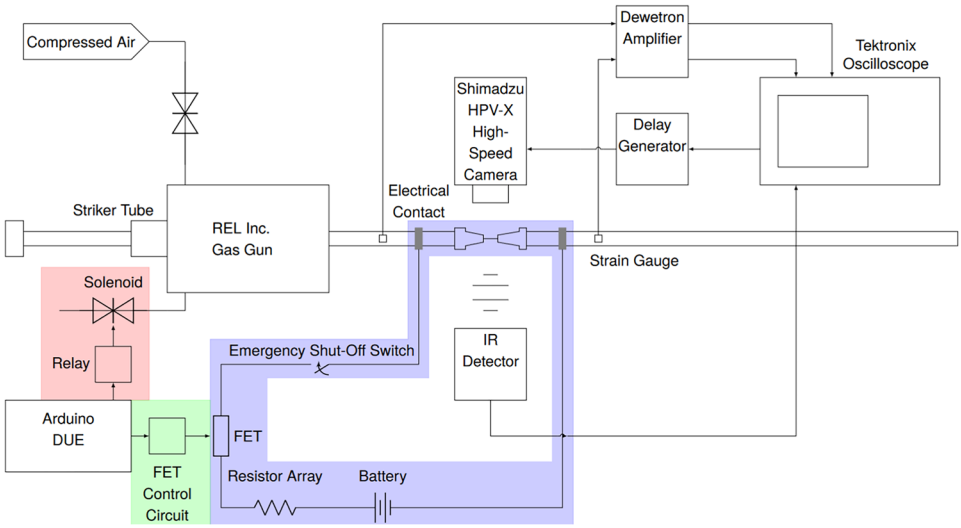

Fig. 2 The TSHPB System in the HSRMML at the University of Utah. The highlighted components are presented in greater detail in Figs. 4, 5, and 6

additional script is used to collect temperature data during heating protocol development testing.

The components of the main heating circuit presented in Fig. 4, starting clockwise from the bottom left, are the power supply, an emergency shut-off switch, a parallel array of resistors in series with FETs. The FETs are connected with Transient Voltage Suppressor (TVS) diodes and FET control inputs, labeled "FET+" and "FET-" in Fig. 4. The circuit is completed through the specimen by attaching welding ground clamps adjacent the grips on the incident and transmitted bar. A nominal $12\,V, 135\,AH$ Absorbent Glass Mat (AGM) battery is used to generate a current through the circuit. AGM batteries feature decreased risk of spillage or off-gassing and lower internal resistance, allowing for high current output. Metal oxide semiconductor FETs are used due to their high current switching capacity and low drain-source resistance in the "on" state (with $6\,V$ applied across the gate and source with the control inputs). The TVS diodes are used as protection against electrostatic discharge that could damage the internal gate capacitors in the FETs. Each resistor array consists of twelve $220\,m\Omega, 100\,W$ resistors, six series-pairs of resistors arranged in parallel, to yield a $73.3\,m\Omega, 1200\,W$ resistor array. These arrays control the maximum current in the circuit, preventing over-current damage through the FETs.

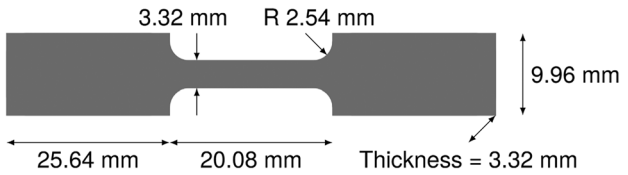

Fig. 3 The tensile specimen dimensions used with the TSHPB

The control circuit, shown in Fig. 5 that provides the FET input voltages uses an Operational Amplifier (Op-Amp) multiplier circuit to proportionally increase the analog voltage signal from the Arduino ($2\,V$) to the required $6\,V$ to energize the FETs. The transistor serves as an additional switch to regulate the control voltage.

The solenoid control circuit is shown in Fig. 6. Here, a digital input from the Arduino actuates a small relay. This relay controls an intermediate, $12\,V$ circuit that energizes a larger, $120\,Vac$ circuit. Finally, the larger relay is used to control the power supply to a solenoid valve. This valve serves as the firing mechanism for the TSHPB gas gun. These relay circuits allow the firing mechanism to be controlled by the same Arduino that governs heating, so the TSHPB gas gun can be fired within milliseconds of the end of the heating process. A delay of $100\,ms$ allows residual electrical fields to settle before testing to avoid any interference with the sensitive strain gauge signals, eliminates the risk of arcing through the specimen, and allows for fields to dissipate to avoid electromechanical effects. Minimizing this delay reduces any subsequent cooling (i.e., cold contact time) so that as deformation begins, the specimen is at the desired testing temperature.

A type-K thermocouple is spot welded to the gauge section of the specimen then connected to a thermocouple meter that serves as an amplifier to measure temperatures. The amplified signal is decreased with a voltage divider to the range of the Arduino analog input.

A voltage of $6.1\,V$ was measured across each of the $73.3\,m\Omega$ resistors during testing, for a total current of $250\,A$

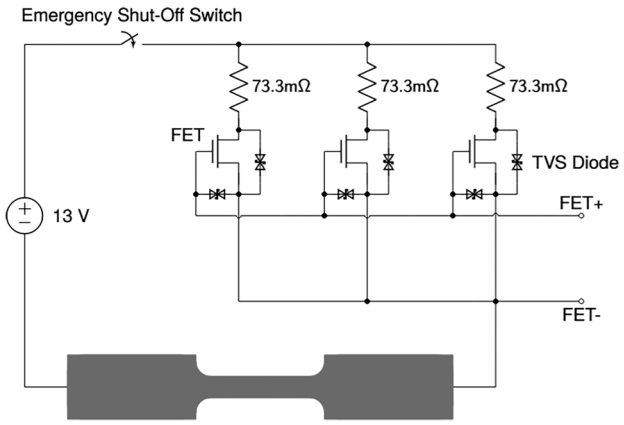

Fig. 4 Main heating circuit

through the specimen that can be maintained continuously for up to 20 seconds. The 250 A current produces heating rates of up to 120 K/s in Ti-6Al-4V samples, measured with the spot-welded thermocouple. Increased current capacity can be easily incorporated by wiring additional resistor arrays and FETs in parallel into the main circuit. However, 250 A is sufficient for present studies.

Heating protocols were developed for each material and each desired temperature. These protocols specify the time and duty cycle for each heating step. For example, the 650 °C heating protocol for Inconel 718 samples requires eight-second heating at 100% duty cycle followed by six-second heating at 60% duty cycle. Heating is conducted at high duty cycles to minimize heating time. Low heating times allow testing of non-equilibrium states and limits bar and clamp heating, preventing any microstructural changes within the TSHPB components. This is of particular concern for the bar materials, C350 maraging steel, to maintain their high strength, and to ensure bar temperatures

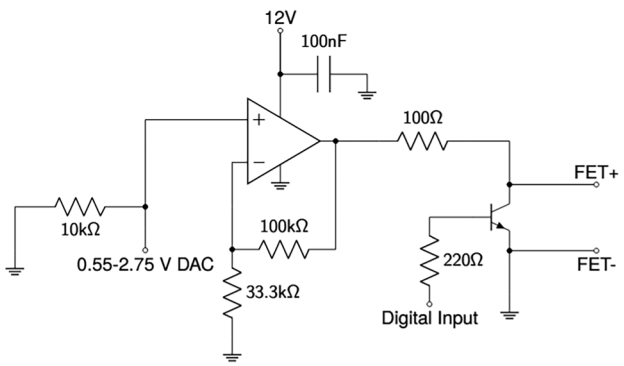

Fig. 5 FET control circuit

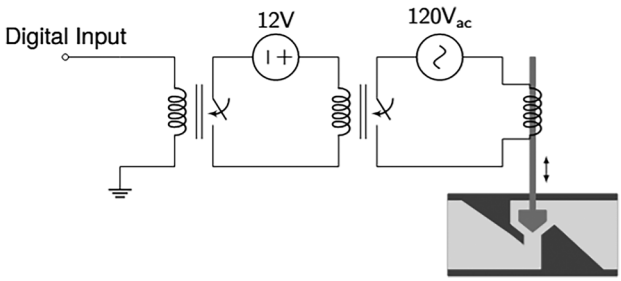

Fig. 6 Solenoid circuit

remain close to room temperature throughout the experiment duration.

Figure 7 shows the timing of events during each experiment. The validated heating protocol is followed by the solenoid trigger, which actuates the gas gun solenoid, firing the striker tube. A Tektronix oscilloscope then collects the strain gauge signals caused by the advancing stress wave.

Results

Multiple heating tests were completed to verify that the duty cycle heating protocols result in repeatable heating profiles up to the desired set temperatures. IR images were taken of the bars and clamps during and after these tests to measure the resulting bar and clamp heating. These images showed that the maximum temperature reached in the bars or clamps was 75 °C, well below the temperatures where the modulus of elasticity or bar speed exhibit temperature dependence or phase transformations could occur in the bars. The temperature profile of an example test performed on Inconel 718 is shown in Fig. 8.

Figure 8(a) shows the entire temperature range of the sample during the heating protocol development. Figure 8(b) shows an enlarged image of the peaks of the temperature profile. The verification tests showed that each of the runs was within 5 °C of the target temperature at the end of the heating, with a standard deviation of 1.34 °C, within the measurement tolerance of the thermocouple used during testing. Similarly, Figs. 9 and 10 show example heating protocols for Ti-6Al-4V (target temperature of 625 °C) and Magnesium AZ31B (target temperature of 275 °C), respectively. The Ti-6Al-4V temperatures after heating had a standard deviation of 1.91 °C and the Magnesium AZ31B tests had a standard deviation of 1.31 °C.

Using the verified heating processes, TSHPB tests were completed with annealed Grade 5 Ti-6Al-4V samples cut from a plate meeting ASTM standard B265. Experiments

Fig. 7 Timing chart of a representative Joule heated TSHPB experiment

were conducted at 20 °C, 450 °C, and 725 °C at a nominal strain-rate of 600 s^{-1} to demonstrate the Joule heating systems capabilities. These results are compiled in Figs. 11 and 12, showing stress-strain curves and strain-rates, respectively.

The triplicate tests show that the experimental setup measured a marked decrease in flow stress as the temperature of the experiment increases. Previous joule heated, dynamic ($\dot{\varepsilon} = 1300\,s^{-1}$) tension studies on heated Ti-6Al-4V performed at Tampere University of Technology in Finland and Technical University of Madrid in Spain found flow stresses of 800 and 600 *MPa* at 450 °C and 700 °C, respectively [45]. Other joule heated, dynamic ($\dot{\varepsilon} = 1000\,s^{-1}$) tension experiments performed at the National Institute of Standards and Technology (NIST) found flow stresses of 1350 and 800 *MPa* at room temperature (20 °C) and 450 °C, respectively [29]. The presented joule heated TSHPB system yields similar results, with our dynamic ($\dot{\varepsilon} = 600\,s^{-1}$) tensile data showing similar values of flow stress of approximately 1300, 750, and 600 *MPa* at room temperature, 450 °C, and 725 °C, respectively. These tests demonstrate the new capability of the HSRMML at the University of Utah to conduct high-strain-rate tension tests at high temperatures.

Discussion

Thorough descriptions of a myriad of SHPB setups used to perform dynamic, elevated temperature experiments are summarized in Refs. [13, 16, 46, 47]. The following discussion will be limited to the several published setups that have similar capabilities as the presented Joule heating system, specifically tensile loading, high heating rates, and unimpeded specimen view during loading. Heated experiments in tension pose unique challenges, so limiting discussion to these systems allows for a more detailed analysis of the utilized solutions. Similarly, it is useful to exclude systems that are not capable of high heating rates (necessary to study non-equilibrium, superheated microstructural states) and which cannot be used in combination

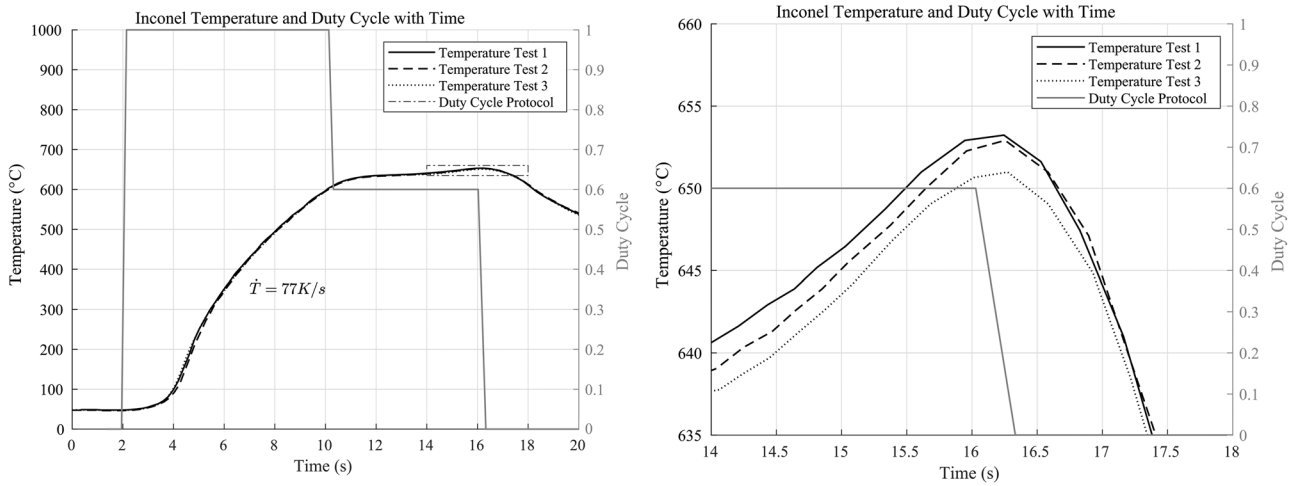

(a) Full Heating Test **(b)** Magnified Heating Test

Fig. 8 Heating test for 650 °C protocol for Inconel 718

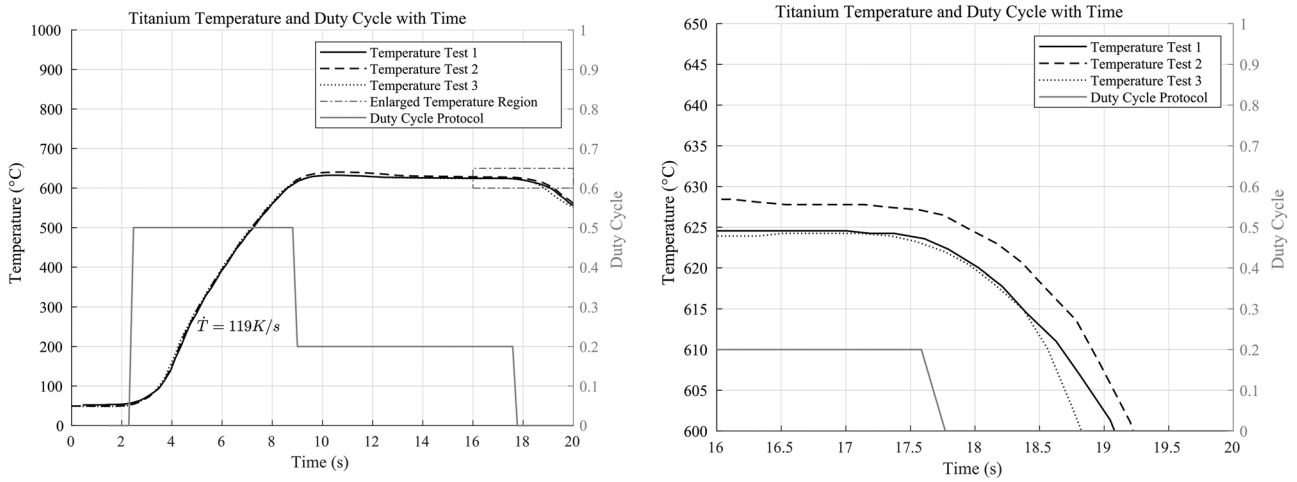

(a) Full Heating Test **(b)** Magnified Heating Test

Fig. 9 Heating test for 625 °C protocol for Ti-6Al-4V

with high speed imaging and IR thermography. Thus, the comparison will include the direct joule heating systems at the Norwegian University of Science and Technology (NTNU) [25], Tampere University of Technology (TUT) in Finland [48], and NIST [7]. Though induction based heating systems can achieve high rate heating, published systems that maintain specimen view have much lower heating rates ($\dot{T} = 10 - 12\,K/s$) [20, 49].

The NTNU heated TSHPB system directly attaches cable eyes to the threaded specimen which is heated with a 220 V powered transformer to provide 200 A of current. The aluminum sample ($A_s = 7\,mm^2$) is heated to 300 °C in ten seconds ($\dot{T} = 28\,K/s$) [46]. The TUT system utilizes specially designed 2 mm sheet specimens ($A_s = 8\,mm^2$) with fins to attach removable copper electrodes [48]. The specimen is glued into the notched bars and the pneumatically actuated electrodes are bought into contact with the fins. A welding transformer provides up to 900 A, resulting in the Ti-6Al-4V sample reaching a temperature of 700 °C in one second ($\dot{T} = 700K/s$) [45]. The NIST system uses an array of batteries to supply a pinned, 1 mm thick specimen ($A_s = 4\,mm$) [29] with 400 A [7], yielding heating up to 1,000 °C in one second ($\dot{T} = 1,000\,K/s$) in the Ti-6Al-4V sample [50]. As

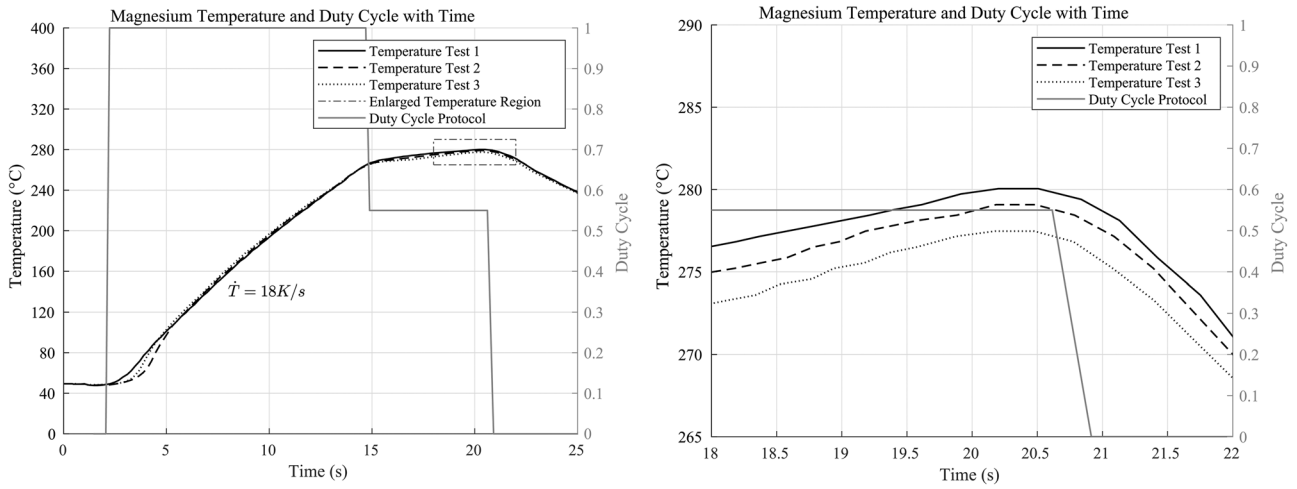

(a) Full Heating Test **(b)** Magnified Heating Test

Fig. 10 Heating test for 275 °C protocol for Magnesium AZ31B

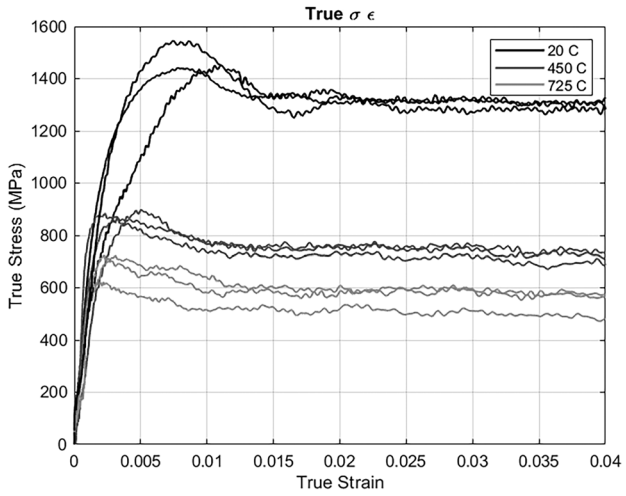

Fig. 11 True Stress strain curves for Ti-6Al-4V Experiments at 20 °C, 450 °C, and 725 °C

described previously, the presented system at the University of Utah produces 250 A through a pressure gripped, square cross-section ($A_s = 11\,mm^2$) Ti-6Al-4V specimen, resulting in heating up to 700 °C in seven seconds ($\dot{T} = 100K/s$). As shown in equation (11), the heating rate is a function of current, specimen geometry, and material. For comparison, the current density through the sample is provided in Table 2.

Although it produces a lower current density, the presented system has still demonstrated its ability to heat a variety of samples to 0.5 T_m in under 20 seconds. Furthermore, the system boasts high-precision heating (±5 °C) without temperature monitoring and feedback during experiments. While a specific temperature precision was not provided for

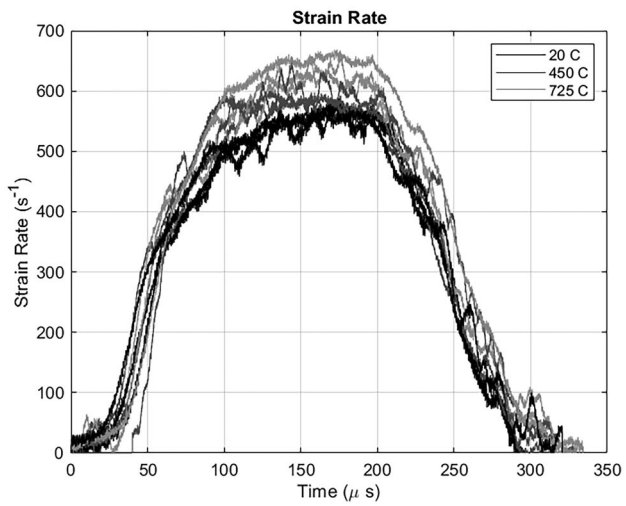

Fig. 12 Strain-rates for Ti-6Al-4V experiments at 20 °C, 450 °C, and 725 °C

Table 2 Current densities generated in selected joule heating systems

System Location	Current Density
Norwegian University of Science and Technology	$29\,A/mm^2$
Tampere University of Technology	$112\,A/mm^2$
NIST	$100\,A/mm^2$
University of Utah	$23\,A/mm^2$

the NTNU system, a calibration experiment showed a 10 °C difference at 300 °C between the contact probe used during experiments and welded thermocouples [25]. The TUT system exhibited an overheat of 22 °C during an example 700 °C target temperature experiment while requiring an attached thermocouple [51]. The NIST system has a reported uncertainty of ±20 °C and requires a near infrared micro pyrometer as a feedback sensor during heating [7]. The NTNU system uses a threaded specimen geometry with variable gauge diameter. Though simple to attach, this geometry significantly complicates DIC and IR thermography as small movements can cause a change of angle in the surface with respect to the camera or detector [25]. Additionally, these specimens require longer, more expensive machining during fabrication. The TUT system has the advantage that the electrical contacts are pneumatically removed before loading [51], so they cannot interrupt the pressure waves during testing (which can result in around 5% error in stress measurements [25]). The application of glue to the specimen and bars (and subsequent cleaning before following experiments) takes considerable time, such that only a few experiments can be completed in a day [45], rather than being able to complete multiple experiments in an hour with other methods. In order for the NIST compression system to achieve its high heating rates, a graphite foil is used to localize heating on the specimen. The addition of the foil requires corrections be made to the data to account for the contribution to the measured behavior [7]. In the tensile setup, precise current control was not possible without a high-resistance foil due to the battery-supplied current and variations in sample and holding assembly resistance [29]. The work presented herein is inspired by and builds upon this previous work, with the objective of demonstrating an agile system capable of rapidly and precisely heating a variety of material specimens up to 0.5 T_m over just a few seconds within a TSHPB.

Conclusions

A new Joule heating system is integrated into the TSHPB system at the University of Utah HSRMML. This integration will allow for material testing to understand the interaction

between temperature and strain-rate of different metallic systems. With the duty-cycled controller, the heating system can quickly and precisely heat a sample to 725 °C for experiments at strain-rates up to $10^3\ s^{-1}$. This apparatus will provide valuable data on the temperature and high-strain-rate dependency of flow stress to be used when modeling machining processes and other high-temperature applications. Experimentation will also allow for further investigations of dislocation activation and plasticity mechanisms' dependence on temperature and strain-rate. The unobstructed view of the specimen during heating and testing will also allow for IR thermography and DIC, which can be used to study Taylor-Quinney heating. These studies will contribute to a more complete constitutive model of material behavior under a broader range of conditions.

Acknowledgements This research was funded by the National Science Foundation CAREER Award No. 1847653. The authors would like to thank S. Mates for many fruitful discussions.

Declarations

Conflicts of Interest The authors have no conflict of interest.

References

1. Lennon AM, Ramesh KT (1998) A technique for measuring the dynamic behavior of materials at high temperatures. Int J Plast 14(12):1279–1292. https://doi.org/10.1016/S0749-6419(98)00056-4
2. Majorell A, Srivatsa S, Picu RC (2002) Mechanical behavior of Ti-6Al-4V at high and moderate temperatures—part i: Experimental results. Materials Science and Engineering: A 326(2):297–305. https://doi.org/10.1016/S0921-5093(01)01507-6
3. Xie Q, Zhu Z, Kang G, Yu C (2016) Crystal plasticity-based impact dynamic constitutive model of magnesium alloy. Int J Mech Sci 119:107–113. https://doi.org/10.1016/j.ijmecsci.2016.10.012
4. Preston DL, Tonks DL, Wallace DC (2003) Model of plastic deformation for extreme loading conditions. J Appl Phys 93(1):211–220. https://doi.org/10.1063/1.1524706
5. Slater NB (1948) Aspects of a theory of unimolecular reaction rates. Proc R Soc Lond A 194(1036):112–131. https://doi.org/10.1098/rspa.1948.0069
6. Song B, Chen W, Antoun BR, Frew DJ (2007) Determination of early flow stress for ductile specimens at high strain rates by using a SHPB. Exp Mech 47(5):671–679. https://doi.org/10.1007/s11340-007-9048-6
7. Mates SP, Rhorer RR, Whitenton E, Burns T, Basak D (2008) A pulse-heated Kolsky bar technique for measuring the flow stress of metals at high loading and heating rates. Exp Mech 48(6):799–807. https://doi.org/10.1007/s11340-008-9137-1
8. Chen R, Xia K, Dai F, Lu F, Luo SN (2009) Determination of dynamic fracture parameters using a semi-circular bend technique in split Hopkinson pressure bar testing. Eng Fract Mech 76(9):1268–1276. https://doi.org/10.1016/j.engfracmech.2009.02.001
9. Lee OS, Kim MS (2003) Dynamic material property characterization by using split Hopkinson pressure bar (SHPB) technique. Nucl Eng Des 226(2):119–125. https://doi.org/10.1016/S0029-5493(03)00189-4
10. Kolsky H (1949) An investigation of the mechanical properties of materials at very high rates of loading. Proc Phys Soc London, Sect B 62(11):676–700. https://doi.org/10.1088/0370-1301/62/11/302
11. Chichili DR, Ramesh KT (1995) Dynamic failure mechanisms in a 6061–T6 Al/Al2o3 metal-matrix composite. Int J Solids Struct 32(17–18):2609–2626. https://doi.org/10.1016/0020-7683(94)00285-5
12. Macdougall DAS, Harding J (1998) The measurement of specimen surface temperature in high-speed tension and torsion tests. Int J Impact Eng 21(6):473–488. https://doi.org/10.1016/S0734-743X(98)00007-4
13. Chen WW, Song B (2010) Split Hopkinson (Kolsky) bar: design, testing and applications. Springer Science & Business Media. https://doi.org/10.1007/978-1-4419-7982-7
14. Corona E (2015) Numerical simulations of the Kolsky compression bar test. Tech. rep., Sandia National Lab.(SNL-NM), Albuquerque, NM (United States). https://doi.org/10.2172/1226520
15. Ravichandran G, Subhash G (1994) Critical appraisal of limiting strain rates for compression testing of ceramics in a split Hopkinson pressure bar. J Am Ceram Soc 77(1):263–267. https://doi.org/10.1111/j.1151-2916.1994.tb06987.x
16. Walley SM (2020) The effect of temperature gradients on elastic wave propagation in split Hopkinson pressure bars. Journal of Dynamic Behavior of Materials 6(3):278–286. https://doi.org/10.1007/s40870-020-00245-9
17. Lindholm US, Yeakley LM (1968) High strain-rate testing: tension and compression. Exp Mech 8(1):1–9. https://doi.org/10.1007/BF02326244
18. Raboin PJ (1989) The mechanical behavior of maraging steel under extreme electromechanical and thermal conditions. PhD thesis, Massachusetts Institute of Technology
19. Tewari R, Mazumder S, Batra IS, Dey GK, Banerjee S (2000) Precipitation in 18 wt% Ni maraging steel of grade 350. Acta Mater 48(5):1187–1200. https://doi.org/10.1016/S1359-6454(99)00370-5
20. Song B, Nelson K, Lipinski R, Bignell J, Ulrich GB, George EP (2015) Dynamic high-temperature tensile characterization of an iridium alloy with Kolsky tension bar techniques. Journal of Dynamic Behavior of Materials 1(3):290–298. https://doi.org/10.1007/s40870-015-0022-6
21. Debta MK, Bishoyi BD, Sabat RK, Muhammad W, Sahoo SK (2020) Microstructure and texture evolution during annealing of Ti-6Al-4V alloy. Mater Sci Technol 36(4):417–424. https://doi.org/10.1080/02670836.2019.1706816
22. Huskins E, Cao B, Li B, Ramesh KT (2012) Temperature-dependent mechanical response of an UFG aluminum alloy at high rates. Exp Mech 52(2):185–194. https://doi.org/10.1007/s11340-011-9565-1
23. Zhang W, Hao P, Liu Y, Shu X (2011) Determination of the dynamic response of Q345 steel materials by using SHPB. Procedia Engineering 24:773–777. https://doi.org/10.1016/j.proeng.2011.11.2735
24. Huo J, He Y, Chen B (2014) Experimental study on impact behaviour of concrete-filled steel tubes at elevated temperatures up to 800 c. Mater Struct 47(1):263–283. https://doi.org/10.1617/s11527-013-0059-8
25. Clausen AH, Auestad T, Berstad T, Børvik T, Langseth M (2006) High-temperature tests on aluminium in a split-Hopkinson bar–experimental set-up and numerical predictions. In: Journal de Physique IV (Proceedings), EDP Sciences vol 134. pp 603–608. https://doi.org/10.1051/jp4:2006134093
26. Rosenberg Z, Dawicke D, Strader E, Bless SJ (1986) A new technique for heating specimens in split-Hopkinson-bar experiments

using induction-coil heaters. Exp Mech 26(3):275–278. https://doi.org/10.1007/BF02320053
27. Abotula S, Shukla A, Chona R (2011) Dynamic constitutive behavior of Hastelloy X under thermo-mechanical loads. J Mater Sci 46(14):4971–4979. https://doi.org/10.1007/s10853-011-5414-y
28. Seo S, Min O, Yang H (2005) Constitutive equation for Ti-6Al-4V at high temperatures measured using the SHPB technique. Int J Impact Eng 31(6):735–754. https://doi.org/10.1016/j.ijimpeng.2004.04.010
29. Kinsey B, Cullen G, Jordan A, Mates S (2013) Investigation of electroplastic effect at high deformation rates for 304SS and Ti-6Al-4V. CIRP Ann 62(1):279–282. https://doi.org/10.1016/j.cirp.2013.03.058
30. Liang C-L, Lin K-L (2018) The microstructure and property variations of metals induced by electric current treatment: a review. Mater Charact 145:545–555. https://doi.org/10.1016/j.matchar.2018.08.058
31. Conrad H (2000) Effects of electric current on solid state phase transformations in metals. Mater Sci Eng, A 287(2):227–237. https://doi.org/10.1016/S0921-5093(00)00780-2
32. Park J-W, Jeong H-J, Jin S-W, Kim M-J, Lee K, Kim JJ, Hong S-T, Han HN (2017) Effect of electric current on recrystallization kinetics in interstitial free steel and AZ31 magnesium alloy. Mater Charact 133:70–76. https://doi.org/10.1016/j.matchar.2017.09.021
33. Hamlin RJ, DuPont JN, Robino CV (2019) Simulation of the precipitation kinetics of maraging stainless steels 17–4 and 13–8+ Mo during multi-pass welding. Metall and Mater Trans A 50(2):719–732. https://doi.org/10.1007/s11661-018-5046-9
34. Maisonnette D, Suery M, Nelias D, Chaudet P, Epicier T (2011) Effects of heat treatments on the microstructure and mechanical properties of a 6061 aluminium alloy. Mater Sci Eng, A 528(6):2718–2724. https://doi.org/10.1016/j.msea.2010.12.011
35. Bolzoni L, Ruiz-Navas EM, Gordo E (2013) Flexural properties, thermal conductivity and electrical resistivity of prealloyed and master alloy addition powder metallurgy Ti-6Al-4V. Mater Des 1980–2015(52):888–895. https://doi.org/10.1016/j.matdes.2013.06.036
36. Rice RC, Jackson JL, Bakuckas J, Thompson S (2003) Metallic materials properties development and standardization (MMPDS). Tech. rep., U.S. Department of Transportation, Federal Aviation Administration
37. Basak D, Overfelt R, Wang D (2003) Measurement of specific heat capacity and electrical resistivity of industrial alloys using pulse heating techniques. Int J Thermophys 24(6):1721–1733. https://doi.org/10.1023/B:IJOT.0000004101.88449.86
38. Pan H, Pan F, Yang R, Peng J, Zhao C, She J, Gao Z, Tang A (2014) Thermal and electrical conductivity of binary magnesium alloys. J Mater Sci 49(8):3107–3124. https://doi.org/10.1007/s10853-013-8012-3
39. Duffy J, Campbell J, Hawley R (1971) On the use of a torsional split Hopkinson bar to study rate effects in 1100–0 aluminum. J Appl Mech 38(1):83. https://doi.org/10.1115/1.3408771
40. Varga J, Kingstedt OT (2021) An investigation of the plastic work to heat conversion of wrought and laser powder bed fusion manufactured Inconel 718. Addit Manuf 46:102179. https://doi.org/10.1016/j.addma.2021.102179
41. Salehi SD, Gilliland W, Kingstedt O (2021) Application of the hough transform for automated analysis of Kolsky bar data. Exp Tech 1–13. https://doi.org/10.1007/s40799-021-00458-0
42. Boyer RR (1996) An overview on the use of titanium in the aerospace industry. Mater Sci Eng, A 213(1–2):103–114. https://doi.org/10.1016/0921-5093(96)10233-1
43. Antunes F, Ferreira J, Branco C (2000) High temperature fatigue crack growth in Inconel 718. Mater High Temp 17(4):439–448. https://doi.org/10.1179/mht.2000.058
44. Lee CA, Lee M-G, Seo OS, Nguyen NT, Kim JH, Kim HY (2015) Cyclic behavior of AZ31B Mg: Experiments and non-isothermal forming simulations. Int J Plast 75:39–62. https://doi.org/10.1016/j.ijplas.2015.06.005
45. Hueto F, Hokka M, Sancho R, Rämö J, Östman K, Gálvez F, Kuokkala VT (2017) High temperature dynamic tension behavior of titanium tested with two different methods. Procedia Engineering 197:130–139. https://doi.org/10.1016/j.proeng.2017.08.089
46. Clausen AH (2018) Tensile testing using the Kolsky-Hopkinson bar machine. In: The Kolsky-Hopkinson Bar Machine. Springer, pp 27–74. https://doi.org/10.1007/978-3-319-71919-1_2
47. Scapin M, Peroni L (2022) 7 - impact and high strain-rate tests at high temperature. In: Song B (ed) Advances in Experimental Impact Mechanics. Elsevier, pp 189–237. https://doi.org/10.1016/B978-0-12-823325-2.00002-9
48. Soares GC, Hokka M (2021) Simultaneous full-field strain and temperature measurements in tensile Hopkinson bar experiments at extreme temperatures. In: EPJ Web of Conferences, EDP Sciences, vol 250. p 01015. https://doi.org/10.1051/epjconf/202125001015
49. Vautrot M, Balland P, Hopperstad OS, Tabourot L, Raujol-Veillé J, Toussaint F (2014) Experimental technique to characterize the plastic behaviour of metallic materials in a wide range of temperatures and strain rates: application to a high-carbon steel. Exp Mech 54(7):1163–1175. https://doi.org/10.1007/s11340-013-9839-x
50. Rhorer R, Mates S, Whitenton E, Burns T (2019) History note: Machining, strain gages, and a pulse-heated Kolsky bar. In: Dynamic Behavior of Materials, vol 1. Springer, pp 95–99. https://doi.org/10.1007/978-3-319-95089-1_15
51. Hokka M, Östman K, Rämö J, Kuokkala V-T (2015) High temperature tension HSB device based on direct electrical heating. In: Dynamic Behavior of Materials, vol 1. Springer, pp 227–233. https://doi.org/10.1007/978-3-319-06995-1_34